

Article

The Magmatic-Hydrothermal Ore-Forming Processes of the Tonggou Cu-Zn Deposit, NW China: Constraints from Magnetite Chemistry and Fluid Inclusions

Chang-Cheng Han ¹, Xue-Bing Zhang ^{1,2,*} , Shi-Shan Wu ¹ and Ying-Ting Liu ¹

¹ College of Geology and Mining Engineering, Xinjiang University, Urumqi 830017, China; hanchangcheng@xju.edu.cn (C.-C.H.); xjuwss@163.com (S.-S.W.); liu_y_t@stu.xju.edu.cn (Y.-T.L.)

² Xinjiang Key Laboratory for Geodynamic Processes and Metallogenic Prognosis of the Central Asian Orogenic Belt, Xinjiang University, Urumqi 830047, China

* Correspondence: zhangxb@xju.edu.cn

Abstract: The Tonggou deposit is a porphyry Cu and vein-type Cu-Zn mineralization system located in the Bogda Orogenic Belt, north of Eastern Tianshan. Systematic fluid inclusion analyses were performed on granular quartz from the magnetite–quartz stage and pyrite–chalcopyrite–quartz stage from the porphyry Cu mineralization. During the early stage of porphyry Cu mineralization, the ore-forming fluids were at high temperatures (450–501 °C) and high salinity (51.2–55.2 wt.% NaCl equiv.) H₂O–NaCl hydrothermal fluids with fluid boiling. These fluids evolved to high temperature (412–450 °C) and intermediate to low salinity (8.3–14.2 wt.% NaCl equiv.) H₂O–NaCl hydrothermal fluids during the pyrite–chalcopyrite–quartz stage. In addition, magnetite from the Tonggou deposit was studied as a marker for the ore-forming process evolution of porphyry and vein-type mineralization. Sampled magnetite can be divided into Mag_I (allotriomorphic magnetite from altered granodiorite), Mag_{II} (magnetite from altered granodiorite found in veinlets or as granular aggregates), Mag_{III} (from the magnetite–quartz stage of porphyry mineralization), and Mag_{IV} (from the polymetallic sulfide–epidote–quartz stage of vein-type mineralization). Magnetite LA-ICP-MS data indicate a hydrothermal origin. The contents of Ti, Si, Al, and Ta are controlled by temperature, and these elements gradually decrease from Mag_I to Mag_{IV}. Moreover, *f*O₂ has considerable influence on the substitution of Sn, V, and Mn in magnetite, and the contents of these elements generally decrease from Mag_I to Mag_{III}—increasing only in Mag_{IV}. Indeed, high *f*O₂ in the polymetallic sulfide–epidote–quartz stage (Mag_{IV}) of vein-type mineralization is shown by the presence of a replacement texture in ilmenite grains within hydrothermal magnetite. On the other hand, magnetite samples from the Tonggou deposit have relatively low Ti + V contents compared to other porphyry Cu deposits—plotting in the skarn field of the (Ti + V) vs. (Ca + Al + Mn) diagram—and shows negative correlations in the (Ti + V) vs. Sn diagram. These data indicate that the porphyry Cu mineralization at Tonggou formed at relatively lower *f*O₂ conditions than the Tonggou vein-type mineralization and other typical porphyry Cu deposits. Finally, porphyry and vein-type mineralization at Tonggou are both sourced from the porphyry system, as a result of ore-forming fluid transfer to a different location.

Keywords: magnetite; trace element composition; fluid inclusion; Tonggou deposit; Eastern Tianshan



Citation: Han, C.-C.; Zhang, X.-B.; Wu, S.-S.; Liu, Y.-T. The Magmatic-Hydrothermal Ore-Forming Processes of the Tonggou Cu-Zn Deposit, NW China: Constraints from Magnetite Chemistry and Fluid Inclusions. *Minerals* **2022**, *12*, 485. <https://doi.org/10.3390/min12040485>

Academic Editor: António Manuel Nunes Mateus

Received: 25 March 2022

Accepted: 13 April 2022

Published: 15 April 2022

Publisher's Note: MDPI stays neutral with regard to jurisdictional claims in published maps and institutional affiliations.



Copyright: © 2022 by the authors. Licensee MDPI, Basel, Switzerland. This article is an open access article distributed under the terms and conditions of the Creative Commons Attribution (CC BY) license (<https://creativecommons.org/licenses/by/4.0/>).

1. Introduction

Magnetite is a common mineral in intermediate to acidic rocks and metallic deposits, which is stable at a wide range of temperatures [1–4]. Indeed, magnetite may display different chemical compositions depending on its formation temperature, mineralization style, and genetic processes involved in its formation. For instance, magnetite crystallized from silicate and sulfide melts at high temperatures is expected to be enriched in Ti, Si, Al, Ba, Ta, Sc, and Y [3]. Thus, due to its wide temperature stability across different ore-forming

processes, magnetite trace element analysis by LA-ICP-MS has increasingly been used to discuss the ore-forming conditions of different deposits [1,4–6].

Based on elemental concentrations and ratios in magnetite, several studies have established geochemical discrimination diagrams for various types of deposits [4,7,8]. On the other hand, some research efforts have been devoted to distinguishing magnetite from igneous, hydrothermal, and sedimentary origins on the basis of elemental variations [1,9,10]. Therefore, some studies have focused on the trace-element geochemistry of magnetite to fingerprint the evolution of the ore-forming hydrothermal fluids and reconstruct the mineralization processes [1,2,11]. However, compositional variations in magnetite from porphyry Cu systems dependent on mineralization style (e.g., porphyry and vein types) are still poorly understood, as are their specific implications for ore-forming conditions and ore-forming fluid evolution. In addition, the study of fluid inclusions is a primary method for getting the information about the ore-forming fluids (e.g., temperatures, salinities, and pressures), which is the key to revealing the ore genesis and ore-forming progress of the hydrothermal deposits [12].

The Tonggou Cu-Zn deposit is located in the Eastern Tianshan section of the Central Asian Orogenic Belt (CAOB)—one of the world’s largest Phanerozoic subduction-accretionary orogens (Figure 1a) [13–15]. This area hosts a number of porphyry Cu deposits, for instance, Tuwu-Yandong, Fuxing, and Sanchakou, located in the Jueluotage Belt [16–18]. Tonggou porphyry Cu and vein-type Cu-Zn mineralization both formed in Late Carboniferous (302–303 Ma; [19,20]), which provide an ideal target to study the chemical variations among different types and generations of magnetite.

This paper presents new magnetite compositional data, acquired using LA-ICP-MS, coupled with a petrographic investigation—i.e., detailed classification and texture analysis from different mineralization stages of the Tonggou deposit. We provide new insight into ore-forming conditions as well as genetic relationships between different mineralization types in porphyry Cu systems. In addition, we acquired fluid inclusion data from porphyry mineralization to constrain the evolution of the ore-forming fluids. The present study could potentially be applied to other similar vein mineralization in porphyry Cu systems.

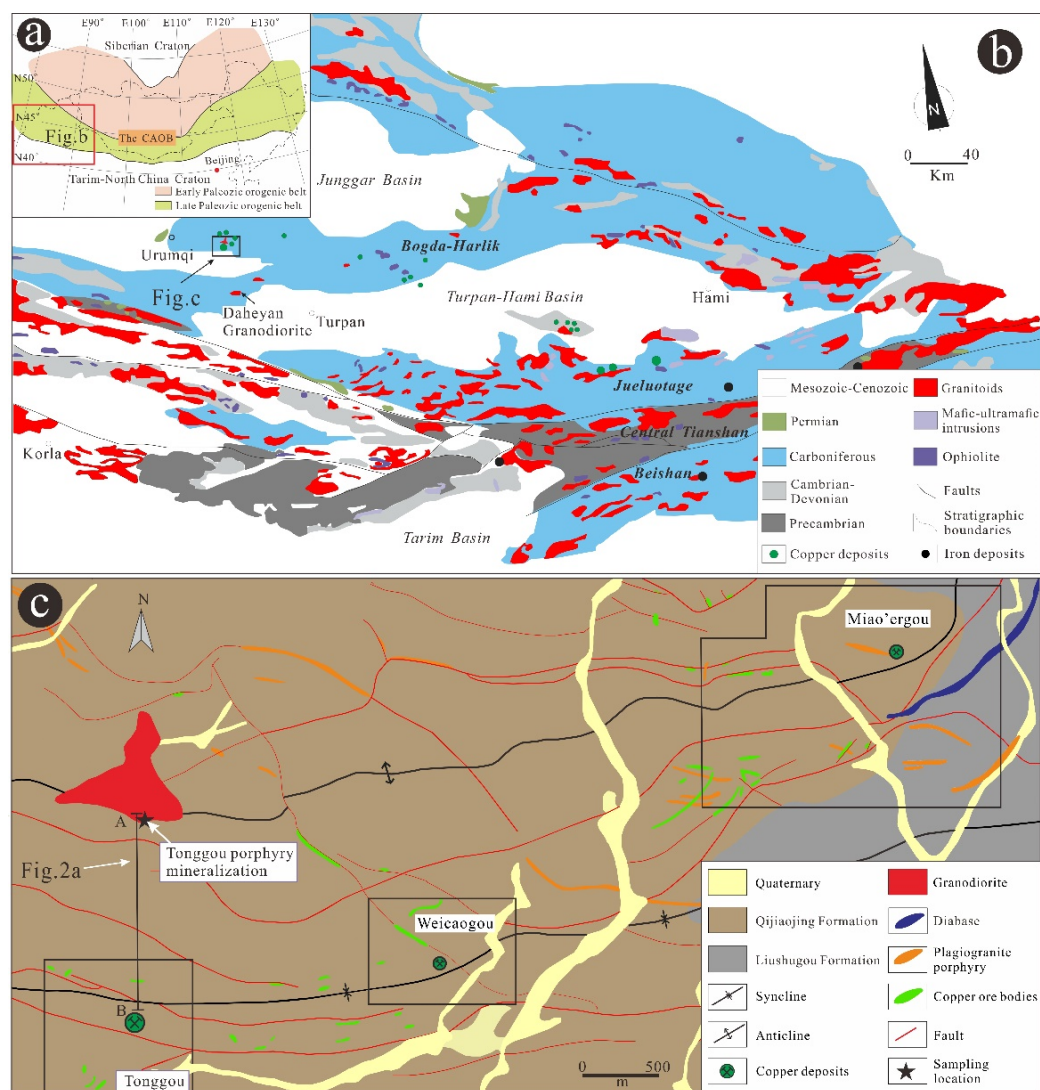


Figure 1. (a) Schematic geologic map of the Central Asian Orogenic Belt (CAOB); (b) geological map of Eastern Tianshan [15]; (c) geological map of the mineralized district in the Tonggou-Miao'ergou area (modified after [20]).

2. Regional Geological Setting

2.1. Regional Geology

The Eastern Tianshan area is located in the southern part of the CAOB, bordered by the Junggar Block to the north and the Precambrian Tarim Block to the south (Figure 1b). Eastern Tianshan can be divided from north to south into the Bogda-Harlik Orogenic Belt, the Jueluotage Belt, the Central Tianshan massif, and the Beishan terrane [21]. This area witnessed the evolution and closure of the Paleo-Asian Ocean [22–24], and the formation of a number of economic Au, Fe, porphyry Cu-Mo, magmatic Cu-Ni, and VMS Cu-polymetallic deposits [25–28]. Porphyry Cu-Mo mineralization in Eastern Tianshan is mainly distributed along the Jueluotage Belt, while the Tonggou porphyry deposit is located in the Bogda Orogenic Belt, with coexisting vein mineralization.

The Bogda Orogenic Belt, situated north of Eastern Tianshan, consists of Devonian, Carboniferous, Permian, and Jurassic strata [29]. The Devonian strata mainly consist of marine and terrigenous sediments, tuffaceous sandstone, and volcanic rocks. The Carboniferous strata show fault contacts with the Devonian rocks and are divided into the Lower Carboniferous Qijiaojing Formation and the Upper Carboniferous Liushugou and Qijiaogou Formations, respectively. The Lower Carboniferous Formation mainly consists of

marine volcanic ignimbrites, tuffaceous sandstone, and bimodal volcanic lavas, while the Upper Carboniferous Formation is dominated by marine (pillow) basaltic lava and felsic ignimbrites, with minor sandstone and siltstone. The Lower and Upper Carboniferous Formations are separated by regional faults. The Permian strata unconformably overlie the Carboniferous rocks and are mainly composed of terrestrial conglomerate, sandstone, and siliceous mudstone, intercalated with bimodal volcanic lavas. In the southeastern region of the study area, Jurassic clastic sediments unconformably overlie the Permian strata [19,29].

Meanwhile, Late Carboniferous to Early Permian intermediate-to-felsic intrusions occur sporadically in the Bogda Orogenic Belt [30–33]. These intermediate-to-felsic intrusions are associated with a series of Cu polymetallic vein deposits [19], such as the Tonggou, Weicaogou, and Miao’ergou deposits (Figure 1c). In addition, porphyry Cu mineralization has been discovered at the top of the Tonggou granodiorite. Moreover, Re-Os and U-Pb isotopic ages indicate that both porphyry and vein Cu polymetallic mineralization at Tonggou formed in the Late Carboniferous (303 Ma, [19,20]).

2.2. Deposit Geology

The Tonggou deposit is located in the western part of the Bogda Orogenic Belt. The exposed strata mainly correspond to the Late Carboniferous Qijiaoqing Formation—consisting of argillite, siltstone, and fine sandstone.

Porphyry Cu mineralization occurs at the top (or contact zone) of the Tonggou granodiorite (Figure 2a). The strata in Tonggou porphyry mineralization belong to the First Segment of Devonian Qijiaoqing Formation and consist of metamorphic fine sandstone and siltstone. Metallic minerals are mainly hematite, magnetite, pyrite, and chalcopyrite (Figure 3a–g), with lesser amounts of galena. Porphyry Cu mineralization mainly occurs as disseminated, veinlet, and stockwork veins, accompanied by potassic and propylitic alteration. Widespread gangue minerals contain abundant K-feldspar, chlorite, epidote, quartz, calcite, and lesser anhydrite. Magnetite is widely present in the porphyry Cu mineralization and is partially replaced by hematite (Figures 3e and 4). Based on mineral assemblages and crosscutting relationships, hydrothermal mineralization at Tonggou can be classified into two stages: the magnetite–quartz stage (stage I) and the pyrite–chalcopyrite–quartz stage (stage II).

Vein-type Cu–Zn mineralization occurs 1.5 km south of the porphyry Cu mineralization and is mainly hosted by Late Carboniferous Qijiaoqing Formation argillite, siltstone, and fine sandstone. The 36 economic ore bodies discovered are mainly distributed in the E–W trend faults, which are widely developed and act as the ore-controlling structures in the Tonggou deposit. For vein-type Cu–Zn mineralization, the shapes and sizes of the ore bodies are controlled by faults, mainly occur as disseminated, veinlet disseminated, lenticular, and vein-shaped [19]. Metallic minerals are mainly magnetite, pyrite, chalcopyrite, and sphalerite, with lesser amounts of hematite, ilmenite, galena, and bornite (Figures 3h,i and 4). Gangue minerals, including quartz, calcite, chlorite, and epidote, occur widely in the Tonggou deposit and are similar to the propylitic alteration of porphyry mineralization [34]. The hydrothermal mineralization at Tonggou can be divided into three stages: the pyrite–quartz stage (stage 1), the polymetallic sulfide–epidote–quartz stage (stage 2), and the pyrite–calcite stage (stage 3).

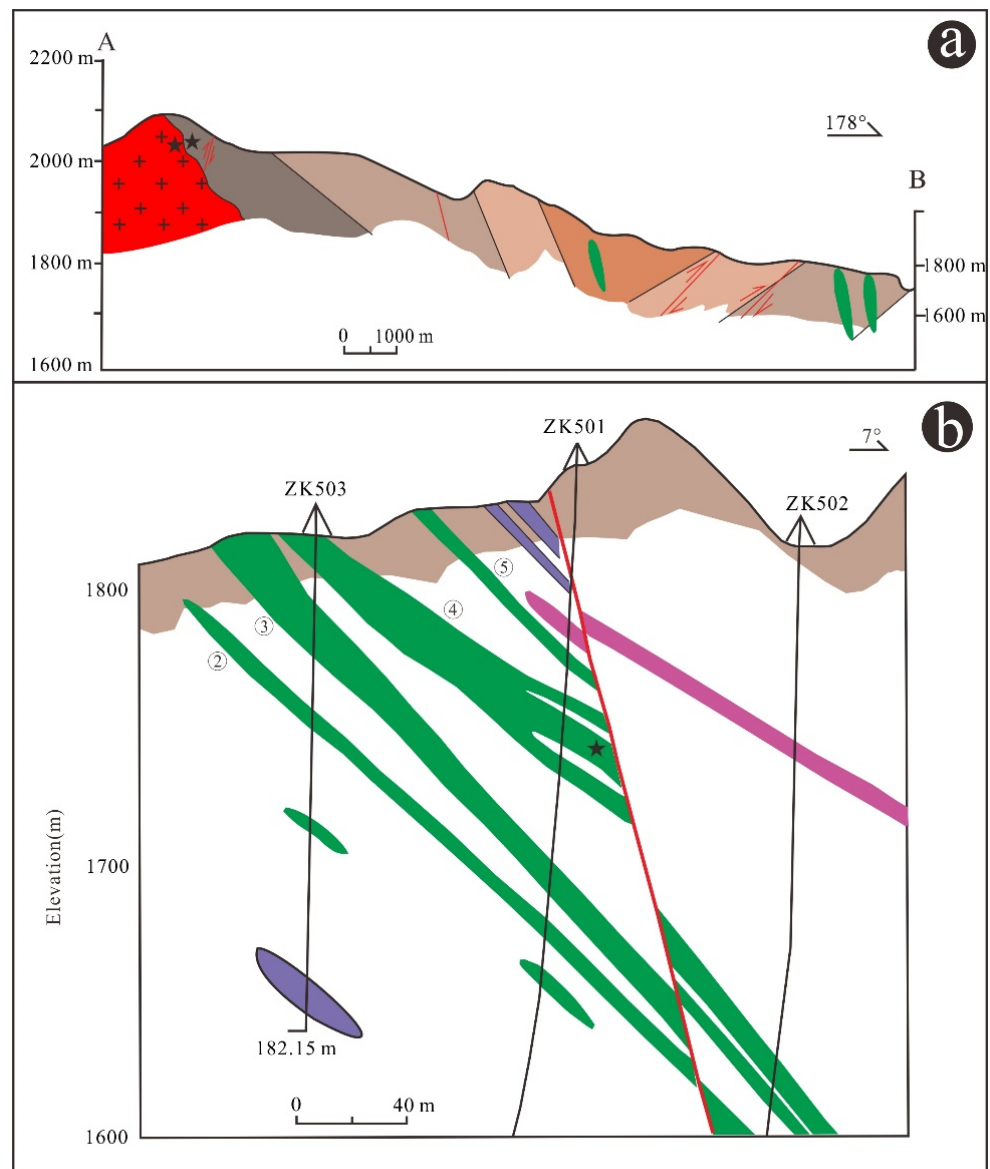


Figure 2. (a) Cross-section of A–B of the Tonggou deposit; (b) cross-section along exploration line 5 of the Tonggou deposit (modified after [32]).

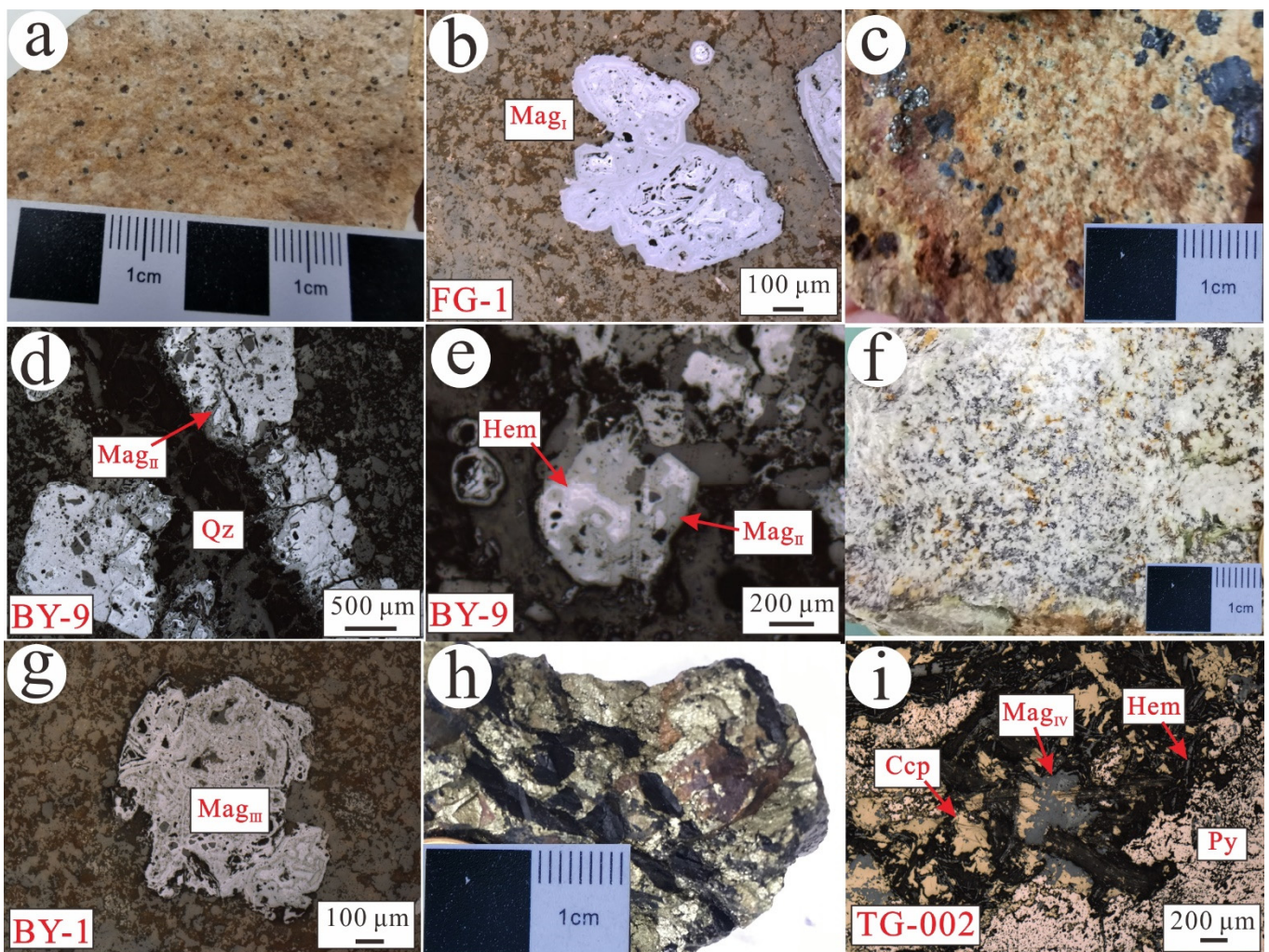


Figure 3. Representative photographs and photomicrographs of magnetite samples at the Tonggou porphyry and vein mineralization. (a) A Mag_I sample from altered granodiorite; (b) reflected-light photomicrograph of Mag_I; (c) A Mag_{II} sample accompanied with pyrite from altered granodiorite; (d) reflected-light photomicrograph of veinlet-disseminated Mag_{II}; (e) reflected-light photomicrograph of euhedral Mag_{II}; (f) A Mag_{III} sample from magnetite-quartz stage; (g) reflected-light photomicrograph of Mag_{III}; (h) the specimen of Mag_{IV} representing polymetallic sulfide-epidote-quartz stage; (i) reflected-light photomicrograph of Mag_{IV}. Ccp—chalcopyrite; Hem—hematite; Mag—magnetite; Py—pyrite; Qz—quartz.

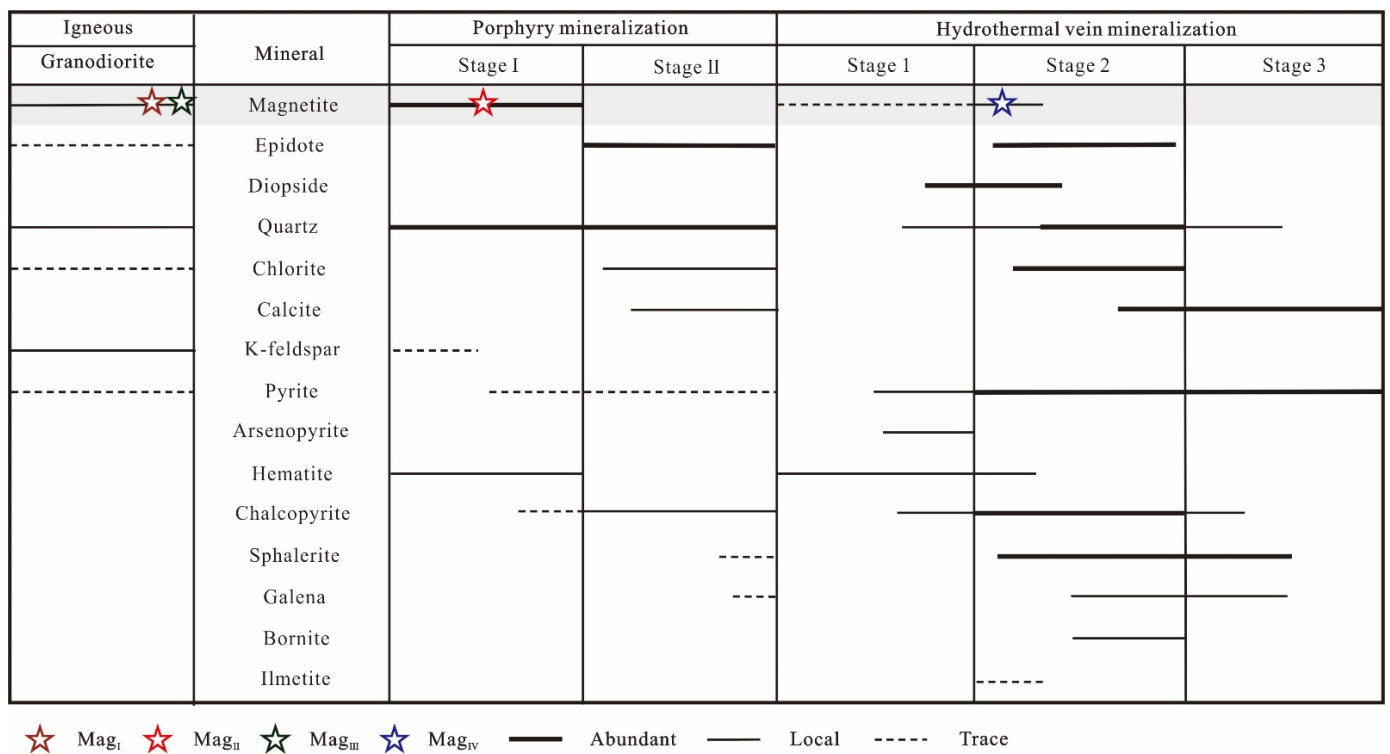


Figure 4. Mineral paragenesis at the Tonggou deposit, showing hydrothermal magnetite.

3. Samples and Analytical Methods

3.1. Sample Preparation

Quartz samples were selected for fluid inclusion analyses, specifically granular quartz from magnetite–quartz stage (stage I) and stage- II pyrite–chalcopyrite–quartz veins (Figure 5a–c). In addition, representative samples were collected from the altered granodiorite and wall rocks of the different mineralization stages. Magnetite samples include two from granodiorite (Mag_I and Mag_{II}), one from stage- I porphyry Cu mineralization (Mag_{III}), and another from stage 2 of vein-type Cu-Zn mineralization (Mag_{IV}). Mag_I from altered granodiorite is allotriomorphic and occurs as isolated or granular aggregates (Figure 3a,b). Mag_{II} from altered granodiorite is subidiomorphic and occurs as veinlet or granular aggregates accompanied by pyrite (Figure 3c–e). Mag_{III} from stage I is allotriomorphic and occurs alongside quartz (Figure 3f,g). Mag_{IV} (stage 2) is allotriomorphic and is partially replaced by chalcopyrite (Figure 3h,i). In addition, some Mag_{IV} samples exhibit ilmenite replacement, which indicates that magnetite from stage 2 formed at high oxygen fugacity conditions.

3.2. Analytical Methods

Fluid inclusion petrography and microthermometric analyses were performed at the Xinjiang Key Laboratory for Geodynamic Processes and Metallogenic Prognosis of the Central Asian Orogenic Belt, Xinjiang University, China. Microthermometric measurements were performed using a Linkam THMS-600 heating-freezing stage mounted on a Carl Zeiss Axiolab microscope with 10× and 50× ultra-long working distance objectives. The heating–freezing rate was generally from 0.2 to 5 °C/min but was reduced to less than 0.2 °C/min near phase transformations. Uncertainties of freezing and heating measurements were ± 0.1 °C from –120 to 31 °C, ± 1 °C from 31 to 300 °C, and ± 2 °C above 300 °C. Homogenization temperature data for fluid inclusions were calculated using the software MacFlincon [35].

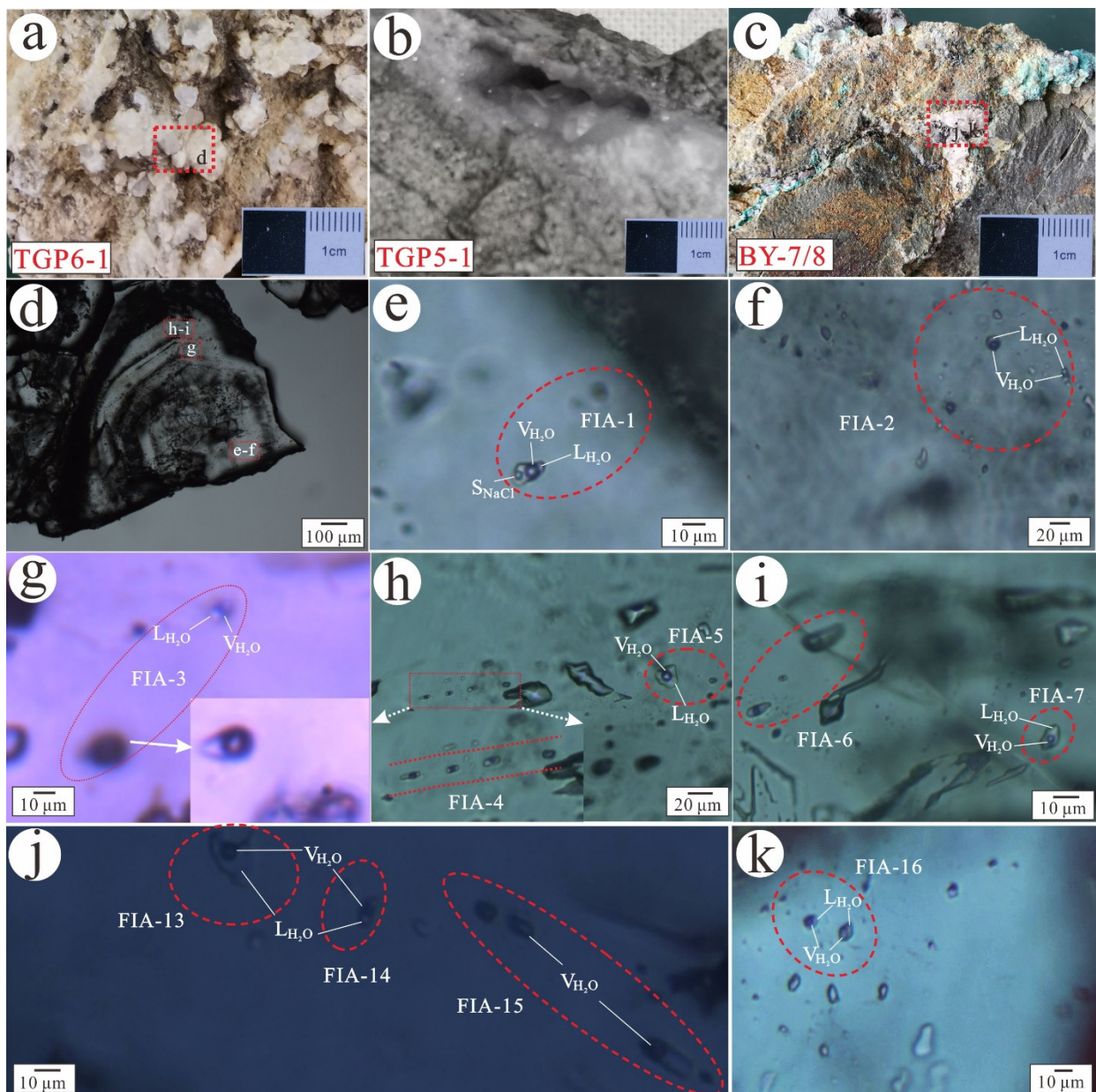


Figure 5. Specimen photographs and photomicrographs of FIAs in quartz from the porphyry Cu mineralization of Tonggou deposit. (a) Granular quartz sample from magnetite–quartz stage; (b) granular quartz vein; (c) chalcopyrite–quartz vein; (d) granular quartz sample from magnetite–quartz stage show growth bands; (e) Boiling FIA (S- and V-type FIAs) in the core of sample TGP6-1; (f) L-type FIA and V-type FIA in the core of sample TGP6-1; (g) L-type FIA and V-type FIA in the transition of sample; (h) L-type FIA and V-type FIA in the rim of sample TGP6-1; (i) L-type FIA in the rim of sample TGP6-1; (j,k) L-type FIA and V-type FIA in sample BY-7; L (liquid phase), V (vapor phase), S (daughter mineral).

Energy dispersive spectrometer (EDS) and back-scattered electron (BSE) analyses were performed on magnetite in the Beijing Kerong Science and Technology Ltd., Beijing, China, prior to LA-ICP-MS analysis. EDS analyses were carried out to obtain Fe, O, Al, Mg, Si, and Ti concentrations, while BSE images were obtained for inclusion identification in magnetite (Figure 6).

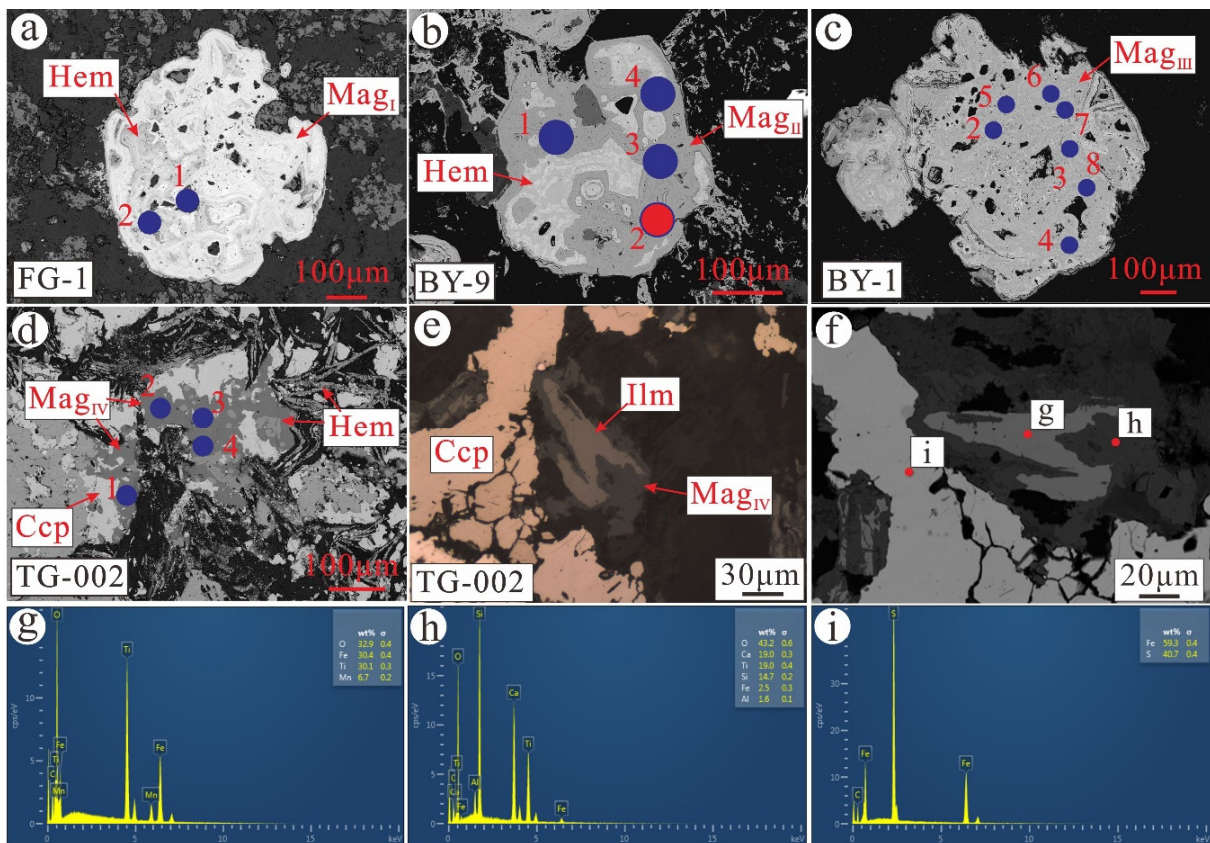


Figure 6. (a) BSE image of Mag_I from sample FG-1; (b) BSE image of Mag_{II} from sample BY-9; (c) BSE image of Mag_{III} from sample BY-1; (d) BSE image of Mag_{IV} from sample TG-002; (e) replacement texture of Mag_{IV} in reflected-light photomicrograph from sample TG-002; (f) replacement texture of Mag_{IV} in BSE image from sample TG-002; (g) EDS analysis on ilmenite; (h) EDS analysis on magnetite; (i) EDS analysis on chalcopyrite.

Trace element analyses of magnetite were performed with LA-ICP-MS at Wuhan Sample Solution Analytical Technology Co., Ltd., Wuhan, China. Detailed operating conditions for the laser ablation system, the ICP-MS instrument, and data reduction are as described by Zong et al. [36]. Laser sampling was performed using a GeolasPro laser ablation system that consists of a COMPexPro 102 ArF excimer laser (wavelength of 193 nm and maximum energy of 200 mJ) and a MicroLas optical system. An Agilent 7900 ICP-MS instrument was used to acquire ion-signal intensities. Helium was applied as a carrier gas. Argon was used as the make-up gas and mixed with the carrier gas via a T-connector before entering the ICP-MS. A “wire” signal smoothing device is included in this laser ablation system [37]. Laser spot size and frequency were set to 44 μm and 5 Hz, respectively. Trace element compositions of magnetite were calibrated against various reference materials (BHVO-2G, BCR-2G, and BIR-1G) without using an internal standard [38]. Each analysis incorporated a background acquisition of approximately 20–30 s followed by 50 s of data acquisition from the sample. The Excel-based software ICPMSDataCal was used to perform off-line selection and integration of background and analyzed signals, time-drift correction, and quantitative calibration for trace element analysis [38].

4. Results

4.1. Petrography of Fluid Inclusions

The standard for distinguishing different generations of FIs within hydrothermal quartz was proposed by Goldstein and Reynolds [39]. FIs along growth bands are considered as separate FIA. Primary FIs occur as isolated inclusions or random groups, while pseudosecondary inclusions are found in infilled internal cracks. Based on fluid inclusion

petrography, three types of fluid inclusions were identified in our samples according to their phase compositions at room temperature (25 °C) and the phase transitions observed during heating and cooling. The three types of inclusions include liquid-rich aqueous inclusions (L), vapor-rich aqueous inclusions (V), and NaCl daughter mineral-bearing three-phase inclusions (S) (Figure 5d–k).

L-type FIAs generally consist of a liquid phase and a minor vapor phase at room temperature, with 10 to 30 vol.% of vapor bubble (Figure 5f–k). With maximum dimensions of 20 μm , these FIAs occur randomly in quartz and are present in granular quartz and stage 2 of porphyry Cu mineralization. VL-type FIAs consist of a liquid with a vapor bubble—which accounts for 60–90% of the FI volume (Figure 5f–h,j,k). This type of FI is typically elliptical and 10–15 μm in size. These FIAs were trapped in granular quartz and stage 2 mineralization and occurred randomly in quartz. S-type FIAs are comprised of halite, liquid phase, and vapor bubble that account for 15–20% of the total volume at room temperature and are generally less than 15 μm in diameter (Figure 5e). This type of FI is only present in the core of granular quartz and is accompanied by minor V-type FIAs.

4.2. Fluid Inclusion Microthermometry

In total, 19 FIAs and 131 FIAs were chosen for microthermometric analysis. Detailed data are listed in Table 1. The homogenization temperature vs. salinity diagram of the different FIAs is presented in Figure 7.

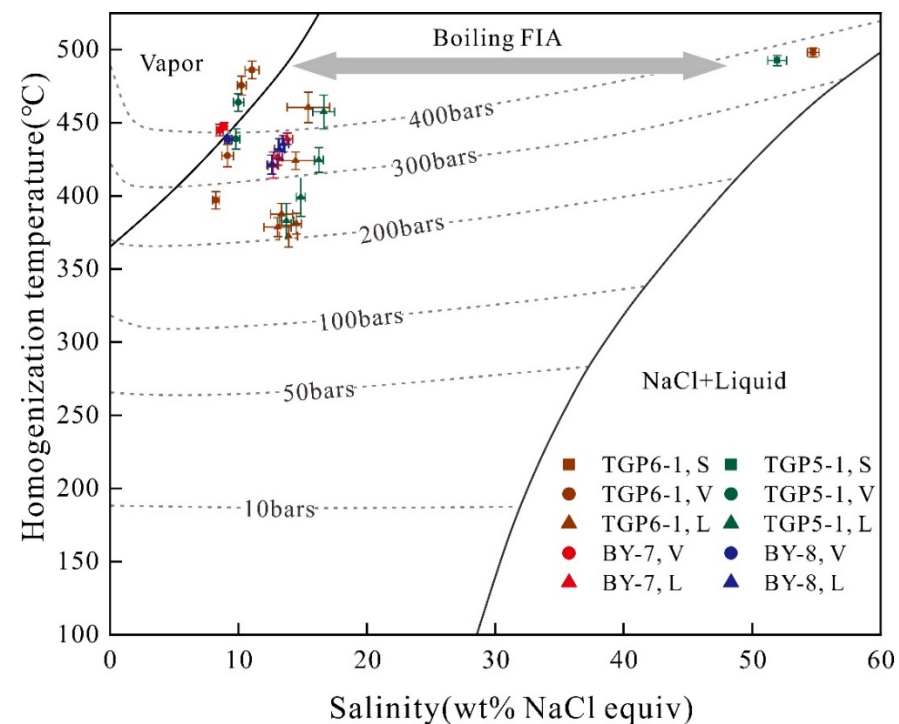


Figure 7. Homogenization temperature vs. salinity in the NaCl–H₂O system for FIAs from porphyry Cu mineralization in the Tonggou deposit. Isobars were calculated using the equations of Driesner and Heinrich [40].

Table 1. Microthermometric data from FIAs in quartz from porphyry Cu mineralization of the Tonggou deposit.

Sample	Host Mineral	FIA	FI Type	Number	Gas–Liquid Ratio (%)	Tm (Ice) (°C)	Tm (NaCl) (°C)	Salinity (wt% NaCl Equiv.)	Th (°C)	Note
TGP6-1	Quartz from granular quartz	FIA-1	V	3	80	From −7.9 to −7.0	458–465	10.5–11.6 (avg.11.1)	480–492	core
			S	2	20			54.3–55.2	495–501	
		FIA-2	V	4	70	From −7.1 to −6.6		9.9–10.6	469–482	
			L	6	15	From −13.1 to −9.8		13.8–17.1	450–471	
		FIA-3	V	3	70	From −6.3 to −5.6		8.7–9.6	420–435	transition
			L	8	20	From −11.9 to −9.1		13.0–15.9	418–430	
		FIA-4	V	2	90	From −5.5 to −5.1		8.0–8.5	391–403	rim
			L	7	25	From −10.2 to −8.7		12.5–14.2	380–395	
FIA-5	L	5	30	From −10.1 to −8.2	12.0–14.1	372–385				
	FIA-6	L	6	20	From −10.6 to −9.3	13.2–14.6	365–380			
	FIA-7	L	5	15	From −10.9 to −10.1	14.1–14.9	374–388			
TGP5-1	Quartz from granular quartz vein	FIA-8	S	3	20		439–445	51.2–52.7	489–496	core
			V	3	80	From −6.9 to −6.3		9.6–10.4	458–470	
		FIA-9	L	7	20	From −13.5 to −11.8		15.8–17.5	446–469	
			V	2	70	From −6.7 to −6.2		9.5–10.1	432–446	transition
		FIA-10	L	6	15	From −12.6 to −11.9		15.9–16.6	416–433	
		FIA-11	L	7	20	From −11.2 to −10.5		14.5–15.2	386–412	rim
	FIA-12	L	5	30	From −10.1 to −9.3	13.2–14.3	371–395	rim		
BY-7	Quartz from pyrite–chalcopyrite–quartz vein	FIA-13	L	6	10	From −9.2 to −8.5		12.3–13.1	412–430	
		FIA-14	L	6	20	From −9.5 to −8.8		12.7–13.4	421–432	
			V	3	80	From −5.7 to −5.3		8.3–8.8	441–449	
		FIA-15	L	8	30	From −10.3 to −9.5		13.4–14.2	435–443	
BY-7	Quartz from pyrite–chalcopyrite–quartz vein	FIA-16	V	2	60	From −5.9 to −5.6		8.7–9.1	445–450	
BY-8	Quartz from pyrite–chalcopyrite–quartz vein	FIA-17	V	3	80	From −6.2 to −5.8		8.9–9.5	436–441	
			L	6	20	From −9.9 to −9.2		13.1–13.9	430–441	
		FIA-18	L	7	15	From −9.6 to −8.9		12.8–13.6	425–439	
		FIA-19	L	6	10	From −9.1 to −8.4		12.2–13.0	415–428	

Granular quartz from porphyry mineralization displays a clearly zonal structure. Grain cores contain abundant L-, V-, and S-type FIs. Final ice-melting temperatures of L-type FIs range from -13.5 °C to -9.8 °C, corresponding to salinities of 13.8–17.5 wt.% NaCl equiv. Total homogenization of L-type FIs to the liquid phase occurred at temperatures of 446–471 °C. Final ice-melting temperatures of V-type FIs range from -7.9 to -6.3 °C, corresponding to salinities of 9.6–11.6 wt.% NaCl equiv. Total homogenization of V-type FIs to the vapor phase occurred at temperatures of 458–492 °C. For S-type FIs, the following homogenization mechanism was observed: halite crystals dissolved first, and the disappearance of the vapor phase occurred later. S-type FIs finally homogenized to a single liquid phase at temperatures of 489–501 °C. Halite crystals within S-type FIs dissolved at temperatures of 439–465 °C, corresponding to salinities of 51.2–55.2 wt.% NaCl equiv.

The granular quartz transition area contains abundant L- and V-type FIs. L-type FIs all homogenize to the liquid phase at temperatures of 416–433 °C. Final ice-melting temperatures of L-type FIs range from -12.6 °C to -9.1 °C, corresponding to salinities of 13.0–16.6 wt.% NaCl equiv. Final ice-melting temperatures of V-type FIs range from -6.7 to -5.6 °C, corresponding to salinities of 8.7–10.1 wt.% NaCl equiv. Total homogenization of V-type FIs to the vapor phase occurred at temperatures of 420–446 °C.

Granular quartz rims also contain abundant L- and V-type FIs. Final ice-melting temperatures of L-type FIs range from -8.2 °C to -11.2 °C. Their salinities are estimated to range between 12.0 and 15.2 wt.% NaCl equiv., and these FIs homogenized to a liquid phase at temperatures ranging from 365 °C to 412 °C. On the other hand, V-type FIs all homogenized to the liquid phase at temperatures of 391–403 °C. Final ice-melting temperatures of L-type FIs range from -5.5 °C to -5.1 °C, corresponding to salinities of 8.0–8.5 wt.% NaCl equiv.

Abundant L- and V-type FIs occur in quartz from stage 2. Final ice-melting temperatures of L-type FIs range from -10.3 °C to -8.4 °C, and their salinities are estimated between 12.2 and 14.2 wt.% NaCl equiv. L-type FIs are homogenized to a liquid phase at temperatures of 412 °C to 443 °C. V-type FIs all homogenize to the liquid phase at temperatures of 436–450 °C. Final ice-melting temperatures of L-type FIs range from -6.2 °C to -5.3 °C, corresponding to salinities of 8.3–9.5 wt.% NaCl equiv.

4.3. Magnetite Chemistry

LA-ICP-MS spot analyses were conducted on four magnetite samples, with two, eight, seven, and eight spots on Mag_I, Mag_{II}, Mag_{III}, and Mag_{IV}, respectively. Representative bulk trace-element compositions (Si, Al, Ti, Mn, Ca, P, Mg, V, Cr, Co, Ni, Cu, Zn, Ga, Zr, Ba, As, Ge, Sn, Sc, Sr, Y, Nb, Mo, W, Hf, Ta, and Bi) are summarized in Table 2. In addition, EDS analyses were conducted to acquire elemental concentrations of ilmenite crystals in magnetite, which show a phenomenon of alteration of the ilmenite (Figure 6e–i).

Table 2. LA-ICP-MS trace element data (ppm) of magnetite from Tonggou deposit.

Sample	Generation	Mg	Al	Si	Ca	Sc	Ti	V	Cr	Mn	Co	Ni	Cu	Zn	Ga	Ge	Sn	W	Pb	Bi
FG1-01	1	1007	10,806	28,084	5225	23.4	723	234	34	471	401.5	470.6	7	590	12.3	6.7	0.9	0.6	8.7	35.7
FG1-02	1	915	8736	18,636	5153	45.3	872	310	136	429	232.4	633.2	6	655	26.2	6.4	0.9	0.9	4.9	3.4
BY-9(1)-01	2	1956	20,850	33,635	4226	37.6	222	356	879	294	7.6	491.1	86	3908	19.1	5.7	0.4	3.4	42.6	4.7
BY-9(1)-02	2	2151	3452	17,063	1316	3.6	19	240	138	534	95.1	732.4	17	1229	2.62	4.9	0.0	0.8	11.9	0.7
BY-9(1)-03	2	1404	20,099	33,527	4561	31.7	319	383	1215	545	7.1	466.8	80	3841	18.9	4.7	1.1	2.8	45.1	2.5
BY-9(1)-04	2	1531	20,763	32,390	4406	34.2	516	342	862	620	7.4	497.8	82	3740	18.2	3.8	0.0	3.0	33.9	2.1
BY-9-01	2	1685	19,564	32,353	4604	34.1	352	347	1008	581	14.9	516.3	75	3232	17.0	5.4	0.6	2.3	28.9	1.9
BY-9-02	2	1817	10,291	26,291	2649	17.5	287	295	685	945	62.1	688.5	47	1909	9.34	5.2	0.0	1.7	23.9	0.7
BY-9-03	2	1864	15,439	31,205	3675	29.9	655	359	381	884	15.8	457.4	59	2629	14.5	6.3	0.2	1.8	38.3	2.9
BY-9-04	2	2002	22,472	40,869	4933	29.8	247	412	1844	617	16.4	606.1	108	3795	27.0	3.6	0.5	3.3	32.0	2.2
BY-1-02	3	623	6285	29,965	777	0.5	294	2	17	518	463.3	761.1	2	261	0.0	2.0	0.5	0.0	2.3	6.4
BY-1-03	3	954	3605	21,831	444	0.6	626	3	13	497	426.6	706.5	2	251	0.2	3.6	1.5	0.1	2.2	4.2
BY-1-04	3	437	1559	21,602	357	0.1	69	1	12	451	552.6	1199.7	5	240	0.0	2.5	0.4	0.0	0.9	1.2
BY1-05	3	585	5391	30,415	668	0.4	280	2	15	367	525.3	885.7	3	206	0.4	3.7	0.4	0.0	1.5	1.4
BY1-06	3	611	3775	23,137	386	0.6	354	2	11	448	451.7	757.2	2	260	0.4	2.6	0.0	0.0	1.6	3.1
BY1-07	3	909	6470	32,784	672	1.0	421	5	19	521	360.1	599.1	1	251	1.0	2.6	0.6	0.1	3.2	7.6
BY1-08	3	618	3371	22,733	548	0.6	380	2	13	371	497.4	826.2	3	254	0.4	5.2	0.2	0.0	1.7	4.2
TG002-2-01	4	2642	5245	15,177	362	4.5	59	30	11	612	2.3	3.9	22,282	481	4.6	41.0	6.2	3023.3	2.1	13.4
TG002-2-02	4	980	2928	9821	249	2.9	18	14	2	498	0.5	0.6	2010	163	2.2	39.0	5.4	3414.5	1.3	4.7
TG002-2-03	4	560	2514	9170	430	2.7	18	24	2	606	4.4	0.3	16,829	217	0.9	32.9	9.4	4653.6	2.6	28.3
TG002-2-04	4	907	1512	15,492	1270	2.5	25	18	8	447	1.9	7.9	10,096	182	1.1	61.8	9.1	5735.6	1.8	15.0
TG002-01	4	400	2351	14,150	561	2.6	41	28	15	487	0.3	0.5	517	151	1.7	76.5	16.2	4616.2	1.7	3.7
TG002-02	4	520	2756	9581	188	3.3	44	24	1	583	1.1	2.9	111	55	1.7	44.7	14.9	4204.6	0.5	10.4
TG002-03	4	482	2332	9911	413	2.6	12	15	27	447	0.4	0.0	58,878	208	1.6	45.3	6.1	3376.0	2.1	14.5

5. Discussion

5.1. Controlling Factors on Magnetite Compositions

Trace elements in magnetite always depend on the formation temperatures of the rock or ore, as well as oxygen fugacity (fO_2), fluid/melt composition, host rock composition, and coexisting minerals during mineral deposit formation [2,4,41]. Titanium is favored in high-temperature ulvospinel–magnetite solid solutions and is incorporated into magnetite by coupling substitution with Fe^{2+} for Fe^{3+} [3,42]). Ti concentrations gradually drop from Mag_I to Mag_{IV} , which is consistent with a higher formation temperature for Mag_{III} (~500 °C, as described in Section 4.2.) than for Mag_{IV} (~400 °C; [19]). These results are coherent with the affinity of magnetite for Ti at higher temperatures. Furthermore, Si, Al, and Ta in magnetite are found to decrease gradually from Mag_I to Mag_{IV} , which implies a positive correlation of these elements with Ti (Figure 8).

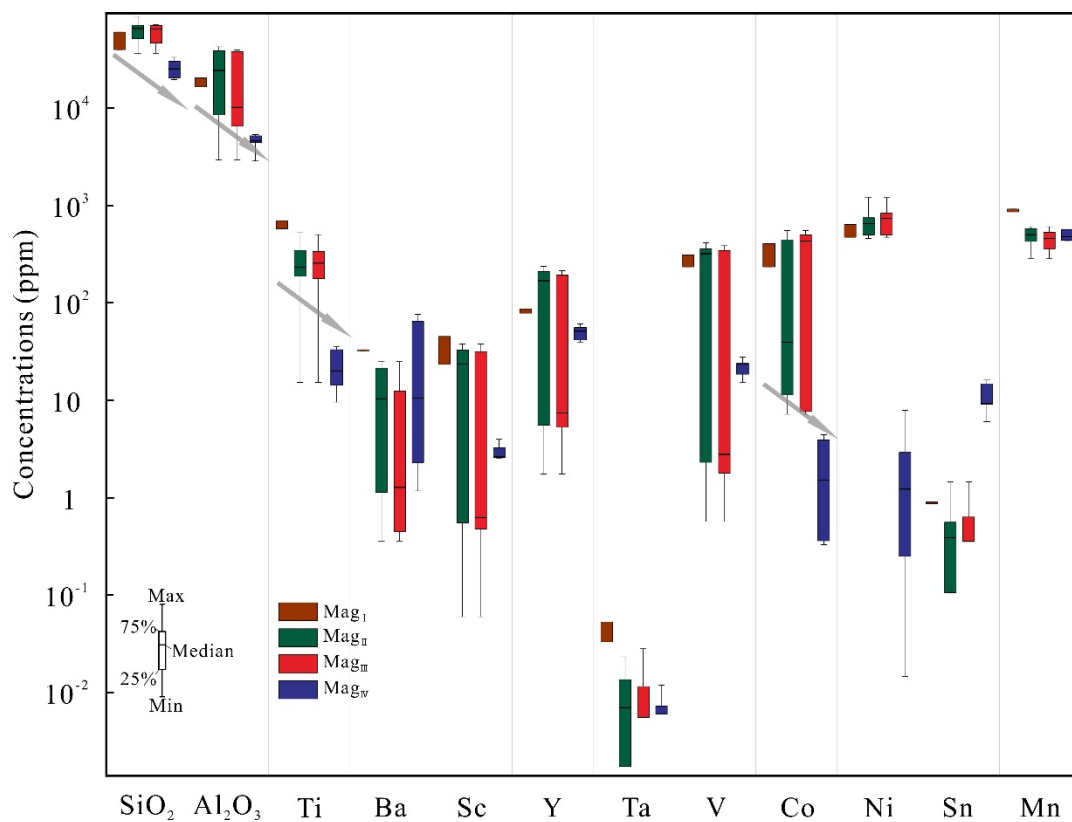


Figure 8. Comparative box plot of SiO_2 , Al_2O_3 , Ti, Ba, Sc, Y, Ta, V, Co, Ni, Sn, and Mn concentrations of the different magnetite generations.

On the other hand, some trace element concentrations (e.g., Sn, V, Mn) are controlled by oxygen fugacity since these elements have several valence states. For instance, in magnetite, Fe^{3+} is substituted by Sn^{4+} more readily than Sn^{2+} [41]. This is consistent with the fact that Mag_{IV} contains higher ratios of Sn than Mag_{III} (Figure 8). In addition, V and Mn generally decrease from Mag_I to Mag_{III} , following the same trend as Ti. However, V and Mn do not decrease with Ti in Mag_{IV} (Figure 8). This can be explained by the appearance of ilmenite replacing Mag_{IV} (Figure 3i), which indicates that high fO_2 is characteristic of stage 2 (polymetallic sulfide–epidote–quartz stage). Thus, Ti in magnetite can be considered a temperature indicator, while Sn, V, and Mn are dependent on both temperature and fO_2 [3,10]

In addition, considering the different partition coefficients of trace elements between magnetite and coexisting minerals, the compositions of certain trace elements in magnetite may also be affected by the co-precipitation of other minerals [1]. For instance, chalcophile

elements (Co, Ni, Cu, Zn, and Bi) partition more readily into sulfides than magnetite [2]. Indeed, there is a decreasing trend in Co, Ni, and Zn contents from Mag_{III} to Mag_{IV} (Figure 8). However, Cu and Bi are not depleted in Mag_{IV} as expected (Figure 8), despite the coexistence of sulfides with Mag_{IV}. It may be a reasonable explanation that Mag_{IV} precipitated earlier than the sulfides, which is supported by the occurrence of secondary chalcopyrite replacing magnetite (Figure 6e). Similar cases have been described in the Yuleken porphyry Cu deposit in East Junggar [4].

5.2. Evolution of Ore-Forming Fluids

FIs identified in the cores of granular quartz grains are LV-, VL-, and S-type FIs with high temperatures (450–501 °C) and high salinity (51.2–55.2 wt.% NaCl equiv.). In addition, fluid boiling occurred in the core of granular quartz, as demonstrated by coexisting vapor-rich (VL-type) and high-salinity (S-type) FIs, which homogenized at similar temperatures, suggesting they were trapped during phase separation [43]. In view of the fact that the homogenization temperature and salinity of boiling FIAs are extremely high (~500 °C), they most likely originated from phase separation of magmatic water due to decompression. In addition, homogenization temperature and salinity decrease gradually from core to rim in granular quartz, which indicates an increasing contribution of meteoric water in ore-forming fluids during the later stage.

On the other hand, FIs from porphyry Cu mineralization (stage 2) have similar homogenization temperatures and salinities to vein-type Cu mineralization in the Tonggou deposit (this study and [19]). In addition, they both formed in Late Carboniferous Porphyry Cu Systems (303 Ma; [19,20]) and occur in adjacent geographical locations. Thus, we consider that the porphyry and vein-type Cu mineralization belong to the same porphyry Cu system.

5.3. Metallogenic Processes

Based on magnetite chemistry, some researchers have proposed discrimination diagrams for distinguishing magnetite of different origins or from various deposit types [1,3,4,7,44]. Tonggou magnetite of different origins was mostly plotted within the magmatic range in the Ni/Cr vs. Ti diagram (Figure 9a). Due to the higher solubility of Ni in hydrothermal fluids with respect to Cr, hydrothermal magnetite has relatively low Ni/Cr ratios [1].

In the (Ti + V) vs. (Ca + Al + Mn) diagram proposed by Dupuis and Beaudoin [7], magnetite from Tonggou plots close to the skarn field (Figure 9b), indicating relatively low Ti + V contents compared to other porphyry Cu deposits. As discussed above, the temperature is a controlling factor for trace element incorporation and correlates positively with Ti, with the early stage of porphyry Cu mineralization showing the highest formation temperatures (~500 °C) and Ti contents of the Tonggou deposit. By observing our data plotted in the (Ti + V) vs. (Ca + Al + Mn) diagram (Figure 9c) by Nadoll et al. [2], it is evident that magnetite from Tonggou is high-temperature magnetite (generally >300 °C). However, V concentrations in Tonggou magnetite are influenced by both temperature and fO_2 and are lower than in other porphyry Cu deposits (e.g., Yuleken Cu deposit; [4]). In addition, zircons from Tonggou granodiorite have high Ce/Ce_N* values (227–234) and Ce⁴⁺/Ce³⁺ ratios (159–286; [20]). Furthermore, Sn is characterized by negative correlations with Ti + V, as seen in the (Ti + V) vs. Sn diagram (Figure 9d). It is worth noting that porphyry Cu mineralization at Tonggou likely formed at relatively high fO_2 conditions, though lower than other porphyry Cu deposits (e.g., Yuleken) and Tonggou vein-type mineralization.

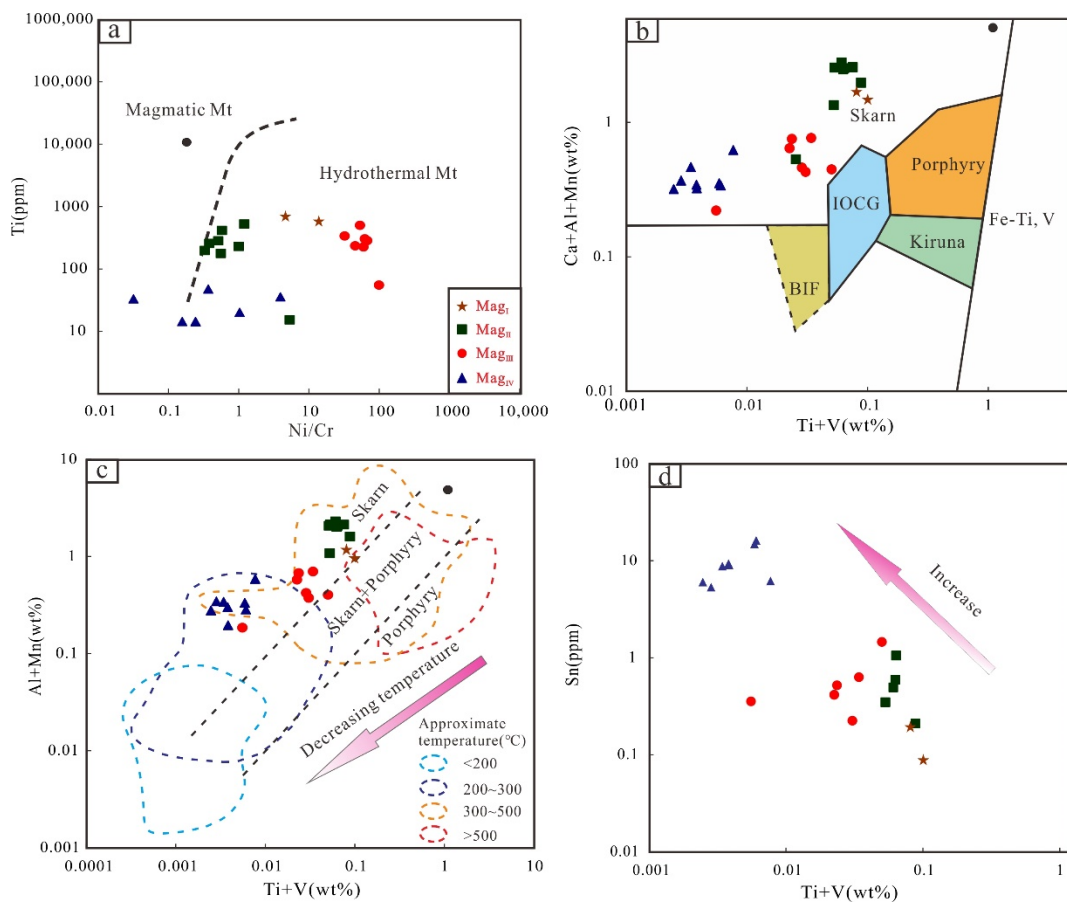


Figure 9. (a) Ti vs. Ni/Cr ratio in magnetite, where the boundary is defined by Dare et al. [1]. (b) (Ca + Al + Mn) vs. (Ti + V) discrimination diagram for magnetite from the Tonggou deposit, where the fields for Kiruna, IOCG, PCD, skarn, Fe-Ti-V, and BIF deposits were defined by Dupuis and Beaudoin [7]. (c) (Al + Mn) vs. (Ti + V) diagram for magnetite (modified after [1]) from the Tonggou deposit. (d) Sn vs. (Ti + V) diagram for magnetite from the Tonggou deposit.

Thus, although both porphyry and vein-type mineralization are sourced from the Tonggou porphyry system, the vein-type mineralization may have formed at a higher fO_2 than the porphyry mineralization. Generally, large and intermediate porphyry Cu deposits are associated with intrusive rocks derived from oxidized magmas [45]. This is consistent with the fact that the vein Cu-Zn mineralization at the Tonggou deposit is economically significant, while the porphyry Cu mineralization is less economically relevant.

6. Conclusions

Magnetite in the Tonggou deposit can be divided into allotriomorphic Mag_I from altered granodiorite, subidiomorphic Mag_{II} from altered granodiorite, allotriomorphic Mag_{III} from the magnetite–quartz stage of porphyry mineralization, and allotriomorphic Mag_{IV} from the polymetallic sulfide–epidote–quartz stage of vein-type mineralization.

LA-ICP-MS analyses reveal that trace elements in magnetite of the Tonggou deposit vary systematically from porphyry to vein-type mineralization. In addition, the content of Ti, Si, Al, and Ta in magnetite is positively correlated with high temperatures, while fO_2 has a considerable influence on Sn, V, and Mn.

Ore-forming fluids of the Tonggou porphyry mineralization were high temperature and high-salinity H_2O -NaCl hydrothermal fluids in the early stage, which derived from a magmatic fluid.

The occurrence of ilmenite replacing Mag_{IV} in the polymetallic sulfide–epidote–quartz stage is characterized by high fO_2 and intermediate to high temperatures. Porphyry and

vein-type mineralization are sourced from the Tonggou porphyry system and are the result of the transfer of ore-forming fluids to a different location.

Author Contributions: Conceptualization, C.-C.H.; Methodology, X.-B.Z.; Software, S.-S.W. and Y.-T.L.; Validation, C.-C.H.; Formal Analysis, X.-B.Z.; Investigation, C.-C.H. and X.-B.Z.; Resources, X.-B.Z.; Data Curation, C.-C.H.; Writing—Original Draft Preparation, X.-B.Z.; Writing—Review and Editing, C.-C.H. and X.-B.Z.; Visualization, X.-B.Z. and S.-S.W.; Supervision, X.-B.Z.; Project Administration, X.-B.Z.; Funding Acquisition, X.-B.Z. All authors have read and agreed to the published version of the manuscript.

Funding: This research was supported by the following funding agency: Tianshan Young Project of Xinjiang, China (Grant No. 2019Q070); the Higher Educational Science and Research Program of Xinjiang, China (Grant No. XJEDU2021Y015); and Students Research Training Program Fund (Grant No. S202010755022).

Data Availability Statement: Not applicable.

Acknowledgments: We are most grateful to the staff of Beijing Kerongen Science and Technology Ltd. for EDS and BSE analysis on magnetite. In addition, we thank the staff of Wuhan Sample Solution Analytical Technology Co., Ltd. for LA-ICP-MS magnetite trace element analysis. We thank the editor and anonymous reviewers for their constructive comments that led to the significant improvement of the manuscript.

Conflicts of Interest: The authors declare no conflict of interest.

References

1. Dare, S.A.S.; Barnes, S.J.; Beaudoin, G.; Méric, J.; Boutroy, E.; Potvin-Doucet, C. Trace elements in magnetite as petrogenetic indicators. *Mineral. Deposita* **2014**, *49*, 785–796. [[CrossRef](#)]
2. Nadoll, P.; Angerer, T.; Mauk, J.L.; French, D.; Walshe, J. The chemistry of hydrothermal magnetite: A review. *Ore Geol. Rev.* **2014**, *61*, 1–32. [[CrossRef](#)]
3. Canil, D.; Grondahl, C.; Lacourse, T.; Pisiak, L.K. Trace elements in magnetite from porphyry Cu-Mo-Au deposits in British Columbia, Canada. *Ore Geol. Rev.* **2016**, *72*, 1116–1128. [[CrossRef](#)]
4. Wu, C.; Chen, H.-Y.; Hong, W.; Li, D.-F.; Liang, P.; Fang, J.; Zhang, L.-J.; Lai, C. Magnetite chemistry and implications for the magmatic-hydrothermal oreforming process: An example from the Devonian Yuleken porphyry Cu system, NW China. *Chem. Geol.* **2019**, *522*, 1–15. [[CrossRef](#)]
5. Huang, X.-W.; Zhou, M.-F.; Qiu, Y.-Z.; Qi, L. In-situ LA-ICP-MS trace elemental analyses of magnetite: The Bayan Obo Fe-REE-Nb deposit, North China. *Ore Geol. Rev.* **2015**, *65*, 884–899. [[CrossRef](#)]
6. Li, D.-F.; Chen, H.-Y.; Hollings, P.; Zhang, L.; Sun, X.-M.; Zheng, Y.; Xia, X.-P.; Xiao, B.; Wang, C.-M.; Fang, J. Trace element geochemistry of magnetite: Implications for ore genesis of the Talate skarn Pb-Zn (-Fe) deposit, Altay, NW China. *Ore Geol. Rev.* **2018**, *100*, 471–482. [[CrossRef](#)]
7. Dupuis, C.; Beaudoin, G. Discriminant diagrams for iron oxide trace element fingerprinting of mineral deposit types. *Mineral. Deposita* **2011**, *46*, 319–335. [[CrossRef](#)]
8. Pisiak, L.K.; Canil, D.; Lacourse, T.; Plouffe, A.; Ferbey, T. Magnetite as an indicator mineral in the exploration of porphyry deposits: A case study in till near the Mount Polley Cu-Au deposit, British Columbia, Canada. *Econ. Geol.* **2017**, *112*, 919–940. [[CrossRef](#)]
9. Chen, W.-T.; Zhou, M.-F.; Gao, J.-F.; Hu, R.-Z. Geochemistry of magnetite from Proterozoic Fe-Cu deposits in the Kangdian metallogenic province, SW China. *Mineral. Deposita* **2015**, *50*, 795–809. [[CrossRef](#)]
10. Chen, W.-T.; Zhou, M.-F.; Li, X.-C.; Gao, J.-F.; Hou, K.-J. In-situ LA-ICP-MS trace elemental analyses of magnetite: Cu-(Au, Fe) deposits in the Khetri copper belt in Rajasthan Province, NW India. *Ore Geol. Rev.* **2015**, *65*, 929–939. [[CrossRef](#)]
11. Liu, Y.; Fan, Y.; Zhou, T.; Xiao, X.; White, N.-C.; Thompsom, J.; Hong, H.; Zhang, L. Geochemical characteristics of magnetite in Longqiao skarn iron deposit in the Middle-Lower Yangtze Metallogenic Belt, Eastern China. *Mineral. Deposita* **2019**, *54*, 1229–1242. [[CrossRef](#)]
12. Ni, P.; Chi, Z.; Pan, J.-Y.; Wang, G.-G.; Chen, H.; Ding, J.-Y. The Characteristics of Ore-Forming Fluids and Mineralization Mechanism in Hydrothermal Deposits: A Case Study of Some Typical Deposits in China. *Bull. Mineral. Petrol. Geochem.* **2018**, *37*, 369–395.
13. Sengör, A.M.C.; Natal'In, B.A.; Burtman, V.S. Evolution of the Altiid tectonic collage and Palaeozoic crustal growth in Eurasia. *Nature* **1993**, *364*, 299–307. [[CrossRef](#)]
14. Jahn, B.M.; Wu, F.; Chen, B. Granitoids of the Central Asian Orogenic Belt and continental growth in the Phanerozoic. *Earth Env. Sci. Trans. R. Soc.* **2000**, *350*, 181–193.
15. Wang, J.-B.; Wang, Y.-W.; He, Z.-J. Ore deposits as a guide to the tectonic evolution in the East Tianshan Mountains, NW China. *Geol. China* **2006**, *33*, 461–469.

16. Wang, Y.-H.; Zhang, F.-F.; Liu, J.-J. Genesis of the Fuxing porphyry Cu deposit in Eastern Tianshan, China: Evidence from fluid inclusions and C-H-O-S-Pb isotope systematics. *Ore Geol. Rev.* **2016**, *79*, 46–61. [[CrossRef](#)]
17. Wang, Y.-F.; Chen, H.-Y.; Baker, M.J.; Han, J.-S.; Xiao, B.; Yang, J.-T.; Fred, J. Multiple mineralization events of the Paleozoic Tuwu porphyry copper deposit, Eastern Tianshan: Evidence from geology, fluid inclusions, sulfur isotopes, and geochronology. *Mineral. Deposita* **2019**, *54*, 1053–1076. [[CrossRef](#)]
18. Zhang, F.-F.; Wang, Y.-H.; Liu, J.-J.; Xue, C.-J.; Wang, J.-P.; Zhang, W.; Li, Y.-Y. Paleozoic Magmatism and Mineralization Potential of the Sanchakou Copper Deposit, Eastern Tianshan, Northwest China: Insights from Geochronology, Mineral Chemistry, and Isotopes. *Econ. Geol.* **2022**, *117*, 165–194. [[CrossRef](#)]
19. Zhang, X.-B.; Chen, C.; Xia, F.; Gao, L.-L.; Quan, H.-Y. Metallogenesis and hydrothermal evolution of the Tonggou Cu deposit in the Eastern Tianshan: Evidence from fluid inclusions, H-O-S isotopes, and Re-Os geochronology. *Geosci. Front.* **2019**, *10*, 2301–2312. [[CrossRef](#)]
20. Zhang, X.-B.; Chai, F.-M.; Chen, C.; Quan, H.-Y.; Wang, K.-Y.; Li, S.-D.; Wu, S.-S. Using whole rock and zircon geochemistry to assess porphyry copper potential of the Tonggou copper deposit, Eastern Tianshan. *Minerals* **2020**, *10*, 584. [[CrossRef](#)]
21. Han, C.-M.; Xiao, W.J.; Wan, B.; Ao, S.-J.; Zhang, J.-E.; Song, D.-F.; Zhang, Z.-Y.; Wang, Z.-M. Late Palaeozoic-Mesozoic endogenetic metallogenic series and geodynamic evolution in the East Tianshan Mountains. *Acta Petrol. Sin.* **2018**, *34*, 1914–1932.
22. Xiao, W.-J.; Zhang, L.-C.; Qin, K.-Z.; Sun, S.; Li, J.-L. Paleozoic accretionary and collisional tectonics of the eastern Tianshan (China): Implications for the continental growth of Central Asia. *Am. J. Sci.* **2004**, *304*, 370–395. [[CrossRef](#)]
23. Wu, F.-Y.; Sun, D.-Y.; Ge, W.-C.; Zhang, Y.-B.; Grant, M.L.; Wilde, S.A.; Jahn, B.M. Geochronology of the Phanerozoic granitoids in northeastern China. *J. Asian Earth Sci.* **2011**, *41*, 1–30. [[CrossRef](#)]
24. Xu, B.; Charvet, J.; Chen, Y.; Zhao, P.; Shi, G.-Z. Middle Paleozoic convergent orogenic belts in western Inner Mongolia (China): Framework, kinematics, geochronology and implications for tectonic evolution of the Central Asian Orogenic Belt. *Gondwana Res.* **2012**, *23*, 1342–1364. [[CrossRef](#)]
25. Mao, J.-W.; Goldfarb, R.T.; Wang, Y.-T.; Hart, C.J.; Wang, Z.-L.; Yang, J.-M. Late Paleozoic base and precious metal deposits, east Tianshan, Xinjiang, China: Characteristics and geodynamic setting. *Episodes* **2005**, *28*, 23–36. [[CrossRef](#)] [[PubMed](#)]
26. Xiao, B.; Chen, H.-Y.; Hollings, P.; Han, J.-S.; Wang, Y.-F.; Yang, J.-T.; Cai, K.-D. Magmatic evolution of the Tuwu-Yandong porphyry Cu belt, NW China: Constraints from geochronology, geochemistry and Sr-Nd-Hf isotopes. *Gondwana Res.* **2017**, *43*, 74–91. [[CrossRef](#)]
27. Zheng, J.-H.; Chai, F.-M.; Feng, W.-Y.; Yang, F.-Q.; Shen, P. Geochemistry and chronology of the early paleozoic diorites and granites in the Huangtupo volcanogenic massive sulfide (VMS) deposit, Eastern Tianshan, NW China: Implications for petrogenesis and geodynamic setting. *Lithos* **2018**, *302–303*, 455–466. [[CrossRef](#)]
28. Zheng, J.-H.; Mao, J.-W.; Yang, F.-Q.; Chai, F.-M.; Shen, P. Petrological and geochemical features of the early Paleozoic granitic gneisses and iron ores in the Tianhu iron deposit, Eastern Tianshan, NW China: Implications for ore genesis. *Lithos* **2017**, *286–287*, 426–439. [[CrossRef](#)]
29. BGMRXUAR (Bureau of Geology and Mineral Resources of Xinjiang Uygur Autonomous Region). *Regional Geology of Xinjiang Autonomous Region*; Geological Memoirs, No. 32, Map Scale 1:500,000; Geological Publishing House: Beijing, China, 1993; pp. 1–841.
30. Gu, L.-X.; Hu, S.-X.; Yu, C.-S.; Li, H.-Y.; Xiao, X.-J.; Yan, Z.-F. Carboniferous volcanites in the Bogda Mountains of eastern Tianshan: Their tectonic implications. *Acta Petrol. Sin.* **2000**, *16*, 305–316.
31. Lei, W.-S.; Xu, P.; Guo, J.-X.; Xiao, L.; Li, X.-C.; Li, Y. LA-ICP-MS zircon U-Pb dating, geological and geochemical features of Sujishan gabbro pluton, eastern Bogda Mountains, and their tectonic significances. *Geol. Rev.* **2016**, *62*, 317–330.
32. Li, P.; Zhu, Z.-X.; Chen, C.; Liu, X.; Chen, B.-X.; Jin, L.-Y.; Huang, L.-M. Geological characteristics and fluid inclusions studies of Tonggou copper deposit of Dabancheng area, Xinjiang. *Xinjiang Geol.* **2015**, *33*, 51–55.
33. Zhang, X.-B.; Chai, F.-M.; Chen, C.; Quan, H.-Y.; Gong, X.-P. Geochronology, geochemistry and tectonic implications of late Carboniferous Daheyen intrusions from the Bogda Mountains, Eastern Tianshan. *Geol. Mag.* **2020**, *157*, 289–306. [[CrossRef](#)]
34. Sillitoe, R.H. Porphyry copper systems. *Econ. Geol.* **2010**, *105*, 3–41. [[CrossRef](#)]
35. Brown, P.E.; Hagemann, S.G. MacFlincor and its application to fluids in Archean lode-gold deposits. *Geochim. Cosmochim. Acta* **1995**, *59*, 3943–3952. [[CrossRef](#)]
36. Zong, K.-Q.; Chen, J.-Y.; Hu, Z.-C.; Liu, Y.-S.; Li, M.; Fan, H.-H.; Meng, Y.-N. In-situ U-Pb dating of uraninite by fs-LA-ICP-MS. *Sci. China Earth Sci.* **2015**, *58*, 1731–1740. [[CrossRef](#)]
37. Hu, Z.-C.; Zhang, W.; Liu, Y.-S.; Gao, S.; Li, M.; Zong, K.-Q.; Chen, H.-H.; Hu, S.-H. “Wave” signal-smoothing and mercury-removing device for laser ablation quadrupole and multiple collector ICPMS analysis: Application to lead isotope analysis. *Anal. Chem.* **2015**, *87*, 1152–1157. [[CrossRef](#)]
38. Liu, Y.-S.; Hu, Z.-C.; Gao, S.; Günther, D.; Xu, J.; Gao, C.-G.; Chen, H.-H. In situ analysis of major and trace elements of anhydrous minerals by LA-ICP-MS without applying an internal standard. *Chem. Geol.* **2008**, *257*, 34–43. [[CrossRef](#)]
39. Goldstein, R.H.; Reynolds, T.J. Systematics of fluid inclusions in diagenetic minerals. *Soc. Sediment. Geol. Sepm Short Course*. **1994**, *31*, 1–199.
40. Driesner, T.; Heinrich, C.A. The system H₂O-NaCl. Part I: Correlation formulae for phase relations in temperature-pressure-composition space from 0 to 1000 °C, 0 to 5000 bar, and 0 to 1 XNaCl. *Geochim. et Cosmochim. Acta* **2007**, *71*, 4880–4901.

41. Carew, M.J. Controls on Cu-Au Mineralization and Fe Oxide Metasomatism in the Eastern Fold Belt, N.W. Ph.D. Thesis, James Cook University, Douglas, QLD, Australia, 2004.
42. Buddington, A.F.; Lindsley, D.H. Iron-titanium oxide minerals and synthetic equivalents. *J. Petrol.* **1964**, *5*, 310–357. [[CrossRef](#)]
43. Ramboz, C.; Pichavant, M.; Weisbrod, A. Fluid immiscibility in natural processes: Use and misuse of fluid inclusion data: II. Interpretation of fluid inclusion data in terms of immiscibility. *Chem. Geol.* **1982**, *37*, 29–48. [[CrossRef](#)]
44. Zhang, Y.; Hollings, P.; Shao, Y.-J.; Li, D.-F.; Chen, H.-Y.; Li, H.-B. Magnetite texture and trace-element geochemistry fingerprint of pulsed mineralization in the Xinqiao Cu-Fe-Au deposit, Eastern China. *Am. Mineral.* **2020**, *105*, 1715–1723. [[CrossRef](#)]
45. Shen, P.; Hattori, K.; Pan, H.-D.; Jackson, S.; Seitmuratova, E. Oxidation condition and metal fertility of granitic magmas: Zircon trace-element data from porphyry Cu deposits in the Central Asian orogenic belt. *Econ. Geol.* **2015**, *110*, 1861–1878. [[CrossRef](#)]